A novel passive structural control device using high-performance NiTiHfPd material

Farzad S. Dizaji[1]

Abstract

This study proposes a super-elastic memory alloy re-centering damper device and investigates its performance in improving the response of steel frame structures subjected to multi-level seismic hazard. The proposed super-elastic memory alloy re-centering damper (SMARD) counts on high-performance shape memory alloy (SMA) bars for re-centering capability and employs friction springs to augment its deformation capacity. An analytical model of six-story steel special moment frame buildings with installed SMARDs is developed to determine the dynamic response of the building. Then, nonlinear response time history analyses are conducted to assess the behavior of controlled and uncontrolled buildings under 44 ground motion records. Results show that SMARDs can enormously mitigate the dynamic response of steel frame structures at different seismic hazard levels and, at the same time, enhance their post-earthquake functionality.

Keywords: Passive Control, Steel Structures, Super-elastic Damper, Earthquake, Shape Memory Alloy, High Performance

1. INTRODUCTION

Conventional seismic design approaches rely on the ability of structures to dissipate the input earthquake energy through inelastic deformations in designed regions of the steel frames, implying substantial structural damage and potential residual drifts after a major earthquake (1). Peak response quantities such as peak story drifts and peak floor acceleration are typically considered to evaluate the performance of different structural systems under seismic loads. However, several studies have shown that residual drifts, which occur due to the nonlinear behavior of yielding components of a structural system, can have an important role in defining the performance of a structure after a seismic event and in the evaluation of potential damage (2, 3).

To enhance the seismic performance of structural systems, structural systems that can provide stable energy dissipation with full self-centering capabilities are desirable. These systems, known as self-centering or re-centering, exhibit flag-shaped hysteric responses with the ability to return to small or zero deformation after each cycle. The self-centering system can control structural damages while minimizing residual drifts. A wide variety of self-centering systems have been developed over the past two decades, including post-tensioned systems, rocking wall systems, and self-centering brace systems (4-9). An extensive review of self-centering systems can be found in (10). Shape memory alloys (SMAs) are a class of smart materials that exhibit unique properties such as excellent re-centering ability, high corrosion and fatigue resistance, and good energy dissipation capacity. These distinct properties of SMA have broadly attracted the attention of researchers to develop SMA-based seismic control systems (11). A number of studies investigated the use of SMAs in developing an effective energy dissipation device with self-centering capabilities (12-17).

To mitigate the adverse effects of dynamic environmental hazards such as earthquakes, strong winds, and hurricanes and achieve a more resilient design under dynamic loads, various passive, active, and semi-active control devices have been proposed and developed (18). The most widely tested and commonly implemented strategies have been passive devices as they are reliable, require no external power, and never destabilize the structure. However, designing buildings with passive systems to provide a performance improvement over all ranges of earthquake and wind excitation is a challenging task.

The application of new materials and/or technology in structural design can help to develop such robust structural systems. Passive energy-dissipating devices that have been intensively investigated during the past decades are among such technologies. A number of passive energy dissipation systems have been developed to mitigate the damaging effects of natural hazards on structures (19-21). Passive energy dissipation devices can be grouped into two main

[1] Corresponding author, Researcher and Lecturer Professor, Department of Engineering & Society, University of Virginia, Charlottesville, VA 22901 (Email: ffs5da@virginia.edu), (Phone Number: +1 321 310 5198)

Active and Passive Smart Structures and Integrated Systems XVI, edited by Jae-Hung Han
Shima Shahab, Jinkyu Yang, Proc. of SPIE Vol. 12043, 120430W
© 2022 SPIE · 0277-786X · doi: 10.1117/12.2614857

Downloaded From: https://www.spiedigitallibrary.org/conference-proceedings-of-spie on 29 Jun 2022
Terms of Use: https://www.spiedigitallibrary.org/terms-of-use

categories: hysteretic devices and rate-dependent devices. Examples of hysteretic devices include metallic yielding devices and friction devices. Energy dissipation in hysteretic devices depends primarily on relative displacements within the device. These devices add initial stiffness until yielding or slip occurs and provide hysteretic energy dissipation. However, they do not provide sufficient damping at small vibrations caused by wind excitation or frequent seismic events while increasing the structure's forces and accelerations due to high stiffness. Furthermore, metallic devices usually have a limited number of working cycles and may require replacement after a strong event, and friction devices may lead to permanent deformations if no restoring force mechanism is provided (22, 23). Examples of rate-dependent devices include fluid viscous dampers and viscoelastic dampers. The energy dissipation capacity of these devices depends on the velocity across the device (21). The viscous damper can provide high force and damping capabilities, while the viscoelastic dampers have a low force and displacement capacity. In general, rate-dependent devices can dissipate energy at all magnitudes of motion but do not possess the same capacity for energy dissipation as hysteretic devices (24). Note that these devices also do not have a self-centering property to return the structure to its original position.

A few additional experts did in-depth numerical and experimental studies to understand the hysteretic behavior of axial dissipaters better. Wang et al. (25) developed an all-steel bamboo-shaped energy dissipator, which consists of an inner bamboo-shaped core and an exterior restraining tube without grouting. The test results demonstrated that the proposed dissipater has a steady tension-compression behavior and good energy dissipation capability. Liu et al. (26) conducted experimental and analytical investigations to further promote the material efficiency of a bamboo-shaped energy dissipater and developed a partially constrained energy dissipater.

Numerous efforts have been carried out to develop new structural systems that can provide stable energy dissipation with full self-centering capabilities (10). Due to its inherent and excellent re-centering ability, high corrosion and fatigue resistance, several researchers have proposed shape memory alloy (SMA)-based seismic protection systems including, but not limited to, SMA-based bracing systems (27, 28); SMA-based dampers (29-32); and SMA-based isolation systems (33-37). Shape memory alloys (SMAs) are a smart class of metallic alloys that have been studied in the design of a number of smart engineered systems (17, 18). Among various SMA compositions, the NiTi alloy has been the most widely studied material for SMA-based dampers. Since NiTi SMAs does not have sufficient energy dissipation capacity to render the use of SMAs as the sole damping device, damping in those devices was supplemented through pre-tensioning SMA elements (38), incorporating a frictional device (39-41), energy-absorbing steel struts (42), viscoelastic device (43, 44), or buckling-restrained braces (45). Wang and Zhu (46) investigated the cyclic behavior of super-elastic SMA bars with buckling-restrained devices under cyclic tension-compression stress. The restraining part of the device was comprised of flat steel plates connected together with two rows of screws. The test findings demonstrated good and stable flag-shaped hysteretic loops with low dependency on loading protocol and strain rate. Qiu et al. (47) introduced a self-centering damper utilizing buckling-restrained super-elastic SMA bars. These bars were either circular form or flat. Grooves were carved out from a length of round bar to make the flat shape bars. The buckling restarting mechanism comprised of a pair of steel plates that were firmly linked through high-strength fasteners. Test results of individual bar specimens demonstrated a steady flag-shaped hysteretic response with a decent self-centering capacity and modest energy dissipation.

A recently developed class of SMAs that consists of NiTiHfPd provides significant energy dissipation and high stresses (48) and can overcome the deficiency of currently available SMAs (49) . Figure 1 presents typical strain-stress diagrams of NiTi and NiTiHfPd SMAs at room temperature. It can be seen that the area captured within the hysteresis loop, which signifies the dissipated energy, for NiTiHfPd is considerably larger than that of NiTi. The strength of NiTiHfPd is also significantly higher than that of NiTi. Thus, the required cross-sectional area of the SMA elements to develop the design force of a damping device will be considerably smaller for NiTiHfPd. A vibration control device based on NiTiHfPd will avoid employing additional energy dissipation units and/or requiring large quantities of material due to the high energy dissipation capabilities and strength of NiTiHfPd. This study discusses the experimental characterization of NiTiHfPd SMAs and conceptual design of a simple but efficient NiTiHfPd SMA-based energy dissipating and re-centering device, which avoids extra fabrication and material costs.

This paper proposes a conceptual design for an innovative SMA-based damper and illustrates its efficiency through numerical simulation of a case study. The Shape Memory Alloy Re-centering Damper (SMARD) combines the energy-dissipating capacity of a cold friction spring with the excellent re-centering properties of SMA bars in a single device, which demonstrates an improved hybrid response. In what follows, the experimental studies on the individual components of the hybrid damper, namely SMA bars and a cold friction spring, are described first. Then, the design and behavior of the proposed super-elastic memory alloy re-centering damper device are introduced. Next, the modeling of SMARD and a six-story and a nine-story steel frame building is discussed. Finally, nonlinear response history analyses are conducted to explore the effectiveness of the SMARD in suppressing the response of the steel building.

Downloaded From: https://www.spiedigitallibrary.org/conference-proceedings-of-spie on 29 Jun 2022
Terms of Use: https://www.spiedigitallibrary.org/terms-of-use

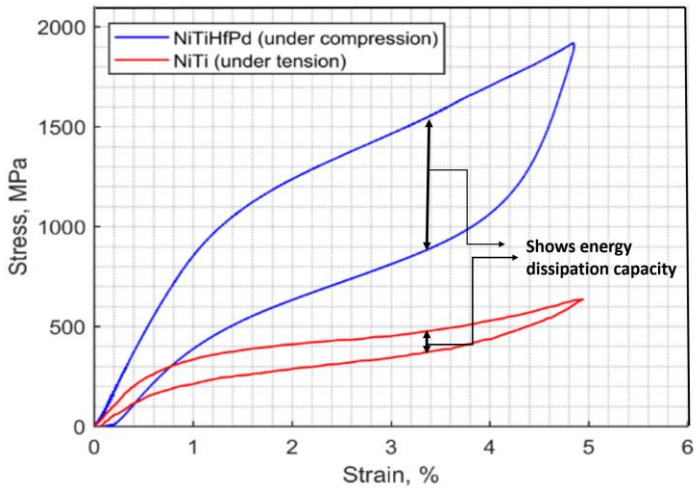
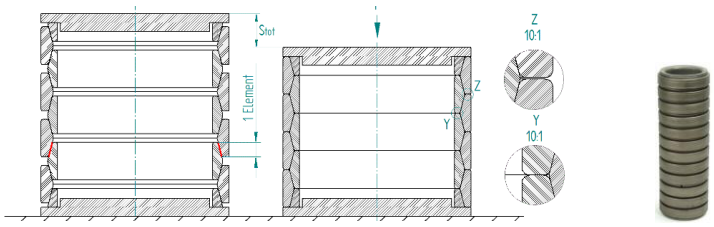


Figure 1. Graph of stress-strain for NiTiHfPd and NiTi at room temperature and loading frequency of 1.0 Hz

2. HIGH DAMPED FRICTION SPRING

Friction springs consist of precisely manufactured outer and inner rings which touch each other on their tapered faces. This contact surface is called an element. Figure 2(a-b) shows a friction spring composed of four outer rings, three inner rings, and two inner ring halves, i.e., the friction spring comprises eight elements. The number of elements is essential for the design of the spring because it determines the total travel and the total spring work. A friction spring works best when it ends with inner ring halves. For this reason, an even number of elements is preferably selected. When the spring column is axially loaded, the tapered surfaces overlap, causing the outer rings to expand and the inner rings to get smaller in diameter. 2/3 of the introduced energy will be absorbed due to friction between the tapered surfaces of the mating rings. Figure 3 shows the basic technical characteristics of friction spring. The selection of the ring size defines further essential parameters for a friction spring; the end force F, The outer and inner guide diameters D_2 and d_2, the element height h_e, the spring travel per element s_e, and the energy absorption per element W_e. For a given application, the required number of elements e is calculated from the desired spring travel or from the required spring work W, while the pre-load is neglected. Finally, the individual rings are built up to form complete spring columns (50).



(a) (b)

Figure 2. (a) Configuration of a friction spring with 8 elements, at rest (left) and loaded (right), (b) friction spring

Downloaded From: https://www.spiedigitallibrary.org/conference-proceedings-of-spie on 29 Jun 2022
Terms of Use: https://www.spiedigitallibrary.org/terms-of-use

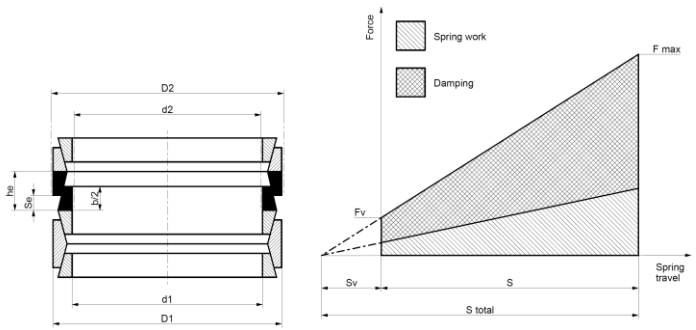


Figure 3. Basic technical characteristics of friction spring

Figure 4 shows experimental test results of the sample friction-spring loaded up to 15 kN and then unloaded. As it can be seen from the results, friction spring has high energy dissipation capacity and is capable of returning to its initial position, which gives the sample excellent re-centering behavior.

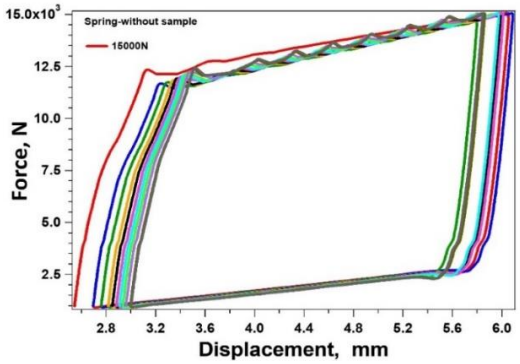
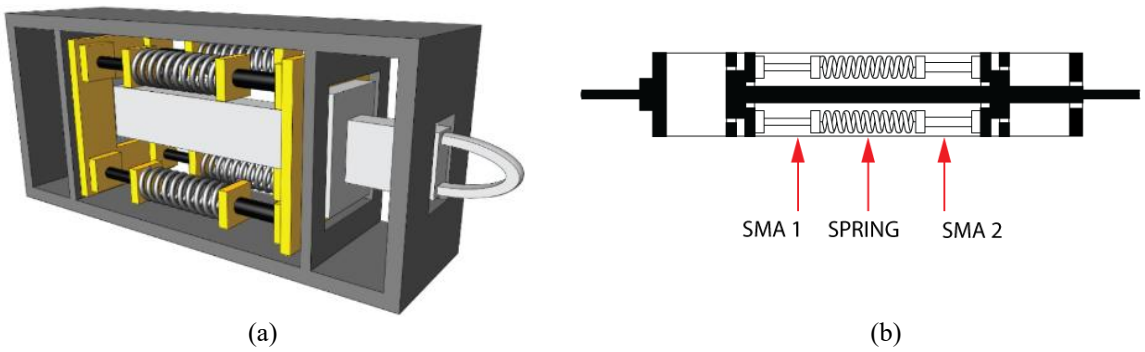


Figure 4. Compression behavior of the friction spring under 15KN

3. SHAPE MEMORY ALLOY-BASED RE-CENTERING DAMPER (SMARD)

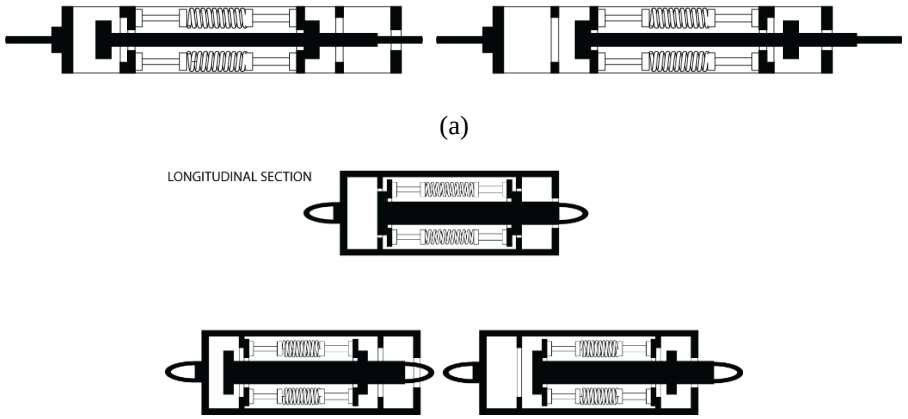
By exploiting the advantageous characteristics of NiTiHfPd SMAs, a new passive vibration device is proposed in this study. The device is named as Shape Memory Alloy-based Re-centering Damper or SMARD. A three-dimensional rendering of the device is also shown in Figure 5a. The SMARD is illustrated with two different diameter bars (SMA1 and SMA2) in Figure 5b. The SMARD comprises an SMA-Spring assembly (rendered in yellow), a piston (gray), and an enclosure (black) with rigidly attached baffle plates. The high force steel springs between SMA groups ensure large displacements under load while simultaneously transmitting the force between SMA groups. Voids in the centers of the baffle plates allow the piston to pass through freely while arresting the otherwise free-traveling SMA-Spring assembly. Note that NiTiHfPd SMAs exhibit better super-elastic response under compression. Therefore, the device is designed such that whether the piston is drawn out of or forced into the device, the SMA-Spring assembly will undergo compression. Due to the inherent super-elastic behavior of NiTiHfPd SMAs, the SMARD can exhibit excellent re-centering ability with enhanced energy dissipation capacity [58].

Downloaded From: https://www.spiedigitallibrary.org/conference-proceedings-of-spie on 29 Jun 2022
Terms of Use: https://www.spiedigitallibrary.org/terms-of-use



(a) (b)

Figure 5. (a) Three-dimensional rendering of SMARD, (b) Plan of the proposed device in its initial position (Saedi et al., 2017).



(a)

(b)

Figure 6. The proposed device: (a) Plan view in its initial and relocated positions (b) Longitudinal view (51)

In addition, SMA bars with up to four different diameters can be incorporated into the device. That will enable the device to produce a damping force that ensures sufficient energy dissipation for various levels of excitation. Figure 6(a-b) shows the plan and longitudinal view of the SMARD at its original and displaced positions to describe its operating principle. As a result of the arrangement of SMA bars in the device and the inherent re-centering behavior of SMAs, a properly designed SMARD will exhibit a re-centering and energy dissipating behavior during all modes of vibrations under both wind and earthquake excitations. During a weak to moderate event, the SMA bars with lower stiffness will experience relatively larger compressive strains and dissipate the energy, while the stiffer SMA bars will undergo small strains. During a moderate to a strong event, both SMA groups will engage and dissipate large amounts of energy, and the device will provide a larger damping force. During an extreme event, the SMARD will stiffen due to the second stiffening of SMA bars under large strains. This additional stiffening will avoid potentially catastrophic structural displacements even under unforeseen strong ground motions (51).

Compared to traditional structural control systems, the suggested SMARD is an attractive alternative in terms of both performance and design efficiency. Due to the high strength of NiTiHfPd SMAs, a compact SMARD device with large force capacities can be efficiently designed by adjusting the total area of SMA bars used in the machine. Here, the prototype SMARD will be designed to have a maximum force capacity of 3600 kN, a stroke of 150 mm, and a loss factor of over 0.30. The loss factor, which is proportional to the device's energy dissipation, is calculated as dissipated energy per cycle (the area within the hysteresis loop) divided by the product of 2π and maximum strain energy (the area under a complete cycle). The target design force can be achieved using four 25-mm diameters in series with another set of four 25-mm diameter NiTiHfPd SMA bars in a single device, assuming the developed alloys will show super-elastic response up to a stress level of 1800 MPa and two different diameter SMA elements are

Downloaded From: https://www.spiedigitallibrary.org/conference-proceedings-of-spie on 29 Jun 2022
Terms of Use: https://www.spiedigitallibrary.org/terms-of-use

employed. It is worth mentioning that a SMARD with different diameters and lengths of SMA bars could be used to modify the damping, force, and stroke capacities of the device. Thus, it provides an ability to tailor the properties of SMARD for specific applications. The SMARD is built for a force capacity of 3600 kN and a displacement capacity of 150 mm in this use. Therefore, the force capacity of the individual SMA bar and single friction spring will be $\frac{3600}{4} = 900\ kN$. To accomplish these layout goals, the SMA bar's cross-sectional region is set to:

$$A_{SingleSMA} = \frac{F}{\sigma} = \frac{900000}{1800} \approx 500\ mm^2$$

Consequently, the diameter of the SMA bar can be calculated as below:

$$A = \frac{\pi D^2}{4}, \qquad D = \sqrt{\frac{4A}{\pi}}, \quad D = \sqrt{\frac{4\,(500)}{\pi}} \approx 25\ mm$$

Using the results of the above calculations, the SMA bar with the diameter of $D = 25\ mm$ is selected. The length of the SMA bars should be designed as well. Since all parts of the SMARD device, two groups of SMAs plus one group of friction springs, will be under compression, the possibility of the buckling for SMA bars should be considered in the design. The length of the SMA bar is also selected to be $L = 200\ mm$ which is a reasonable length for the SMA bar to be a part of a system. In order to avoid buckling, the following inequality must be satisfied:

$$P_{cr} = \frac{\pi^2 .\ E\ .\ I}{(k\ .\ L)^2} > 900\ kN$$

Where P_{cr} Stands for buckling force, E is the module of elasticity for the SMA bar, I is a moment of inertia for the circle area of the SMA bar, $(k\ .\ L)$ is the effective length of the SMA sample bar, L is the length of a single SMA bar, and k column effective length factor that must be obtained for different types of supports or endpoints. Since two endpoints of the attached SMA bar to the plates will have to be restrained completely (no rotation and displacement), the value of k should be selected to be 0.5. What's more, the moment of inertia can be calculated using the following formula for the circle area of the SMA bar:

$$I_x = I_y = \frac{\pi R^4}{4}\ (mm)^4, \quad R = \frac{D}{2}\ mm, \qquad R = \frac{25}{2} = 12.5\ mm, \quad I_x = I_y = \frac{\pi\ (12.5)^4}{4} = 19165\ (mm)^4$$

The module of elasticity for the SMA bar can be obtained from the formula below using Figure 7.

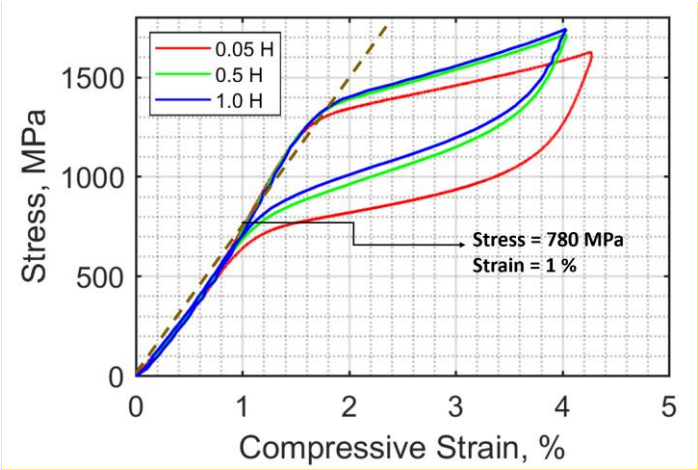


Figure 7. Stress-strain plots of SMA NiTiHfPd bars in different frequency loads

Downloaded From: https://www.spiedigitallibrary.org/conference-proceedings-of-spie on 29 Jun 2022
Terms of Use: https://www.spiedigitallibrary.org/terms-of-use

$$E = \frac{\sigma\,(stress)}{\varepsilon\,(strain)} = \frac{780}{0.01} = 78000\ MPa$$

Furthermore, the experimental data of the SMA bar for the temperature room (25°C) was used for the design of the device. Therefore, in order to find the elasticity module of the SMA bar stress-strain plot of Figure 7 was considered. Additionally, since the earthquake frequencies are usually close to 1.0 Hz, the experimental data of the SMA bar with the frequency of 1.0 Hz was utilized for the damper. Finally, the critical force for the SMA bar can be obtained from the formula below:

$$P_{cr} = \frac{\pi^2 \times\ (78000) \times\ 19165}{(0.5 \times 200)^2} = \ 1473\ kN > 900\ kN$$

The critical force of the SMA bar under compression is greater than the design force for each SMA bar. Therefore, the SMA bar will not buckle under compression. The cross-sectional region chosen corresponds to two groups of four collection SMA bars, each with a diameter of 25 mm.

Moreover, the behavior of the numerical model of the spring at large displacement levels with the experimental behavior of the spring at large displacement levels (i.e., the blue line in Figure 8(a-b) below) are compared in Figure 8(c). Our numerical model seems to correctly model the spring behavior. Since the device will have a force capacity of 3600 kN, four friction-springs with a force capacity of 900 kN each will be assembled in parallel with each other in the middle part of the device. The mechanical characteristics of the spring can be obtained accordingly. Our spring consists of 12 elements, type 24301. The deformation capacity of the single spring will be: 12.0 x 8.0 (S_e) = 96.0 mm, spring work (absorbed energy) will be: W_e = 3708.0 x 12 = 44496 J, spring length will be: 12 x 33.3 (h_e) = 400 mm. By adding additional elements, the stroke (length of the spring), the absorbed energy (spring work) will be increased consequently, but the end force will remain the same, which is 900 kN for selected friction spring. To achieve optimum stroke power, the friction spring must be 400 mm in length (52).

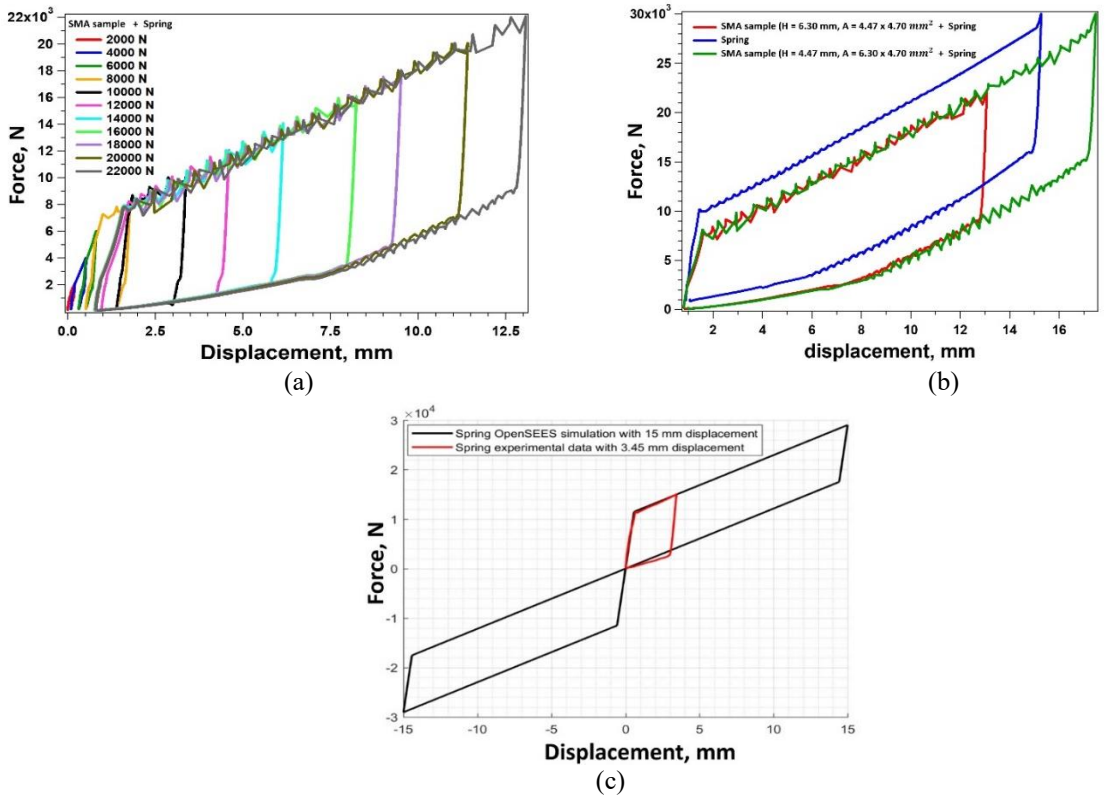


Figure 8. (a) Compression behavior of friction spring in series with SMA sample loaded up to 22 kN and unloaded in room temperature, (b) comparison of the SMA sample and friction-spring loaded up to 30 kN (c) Opensees simulation of friction spring sample

Downloaded From: https://www.spiedigitallibrary.org/conference-proceedings-of-spie on 29 Jun 2022
Terms of Use: https://www.spiedigitallibrary.org/terms-of-use

4. STEEL MOMENT FRAME WITH INSTALLED SMARDs

4.1. Building description (A six-story building)

In order to evaluate the performance of the proposed damper in mitigating the seismic response of structures, two special steel moment resisting frames are chosen for this purpose. A six-story steel building illustrated in the FEMA P-751, NEHRP Recommended Seismic Provisions: Design Examples (53) is selected for numerical analyses. The building is designed as an office building located in Seattle, Washington, on class C soil. The special steel moment-resisting frames on the perimeter of the building provide the lateral load resistance for the structure. The building consists of five bays at 8.53 m (28 feet) in the north-south (N–S) direction and six bays at 9.14 m (30 feet) in the east-west (E–W) direction. A plan and elevation of the building in the N–S direction are shown in Figure 9(a-b). All the analyses in this study are for lateral loads acting in the N–S direction. The story height is 3.81 m (12 feet-6 in.) on each floor except the first floor, which has a height of 4.57 m (15 feet). One of the perimeter steel special moment frames that serve as the seismic-force-resisting system of the structure is analyzed. All the columns in the N–S direction bend about their strong axis, and the girders are attached with fully welded moment-resisting connections. The building is designed with Reduced Beam Section (RBS) connection details in accordance with design standards, ASCE/SEI 7-05 (54) and ANSI/AISC 341-05 (55). The RBS variables were obtained manually then the necessary variables were entered into Opensees programming. As a matter of fact, this is the reason the RBS is used to reduce the stress concentration at the column panel zones, and they are expected to yield during seismic excitation. The reduced beam section basically protects a welded SMARF connection detail by forcing the plastic hinge in a beam to form away from the column face. The building is assigned to Seismic Design Category (SDC) D.

The design spectral acceleration parameters are S_{DS} = 0.912 g and S_{D1} = 0.459 g, while the maximum considered spectral acceleration values are S_{MS} = 1.368 g and S_{M1} = 0.689 g. The seismic mass of the second level is 1.248 x 10^6 kg, the mass of the third level to the sixth level is 1.242 x 10^6 kg, and the mass of the roof level is 1.237 x 10^6 kg. The fundamental period of the structure is 2.04 s. The building was analyzed in FEMA P-751 through a nonlinear response history analysis, and excessive story drifts were identified, especially at lower floor levels. A damping system was suggested to upgrade the performance of the structure. In this study, super-elastic viscous dampers will be installed to enhance the seismic response of the selected building.

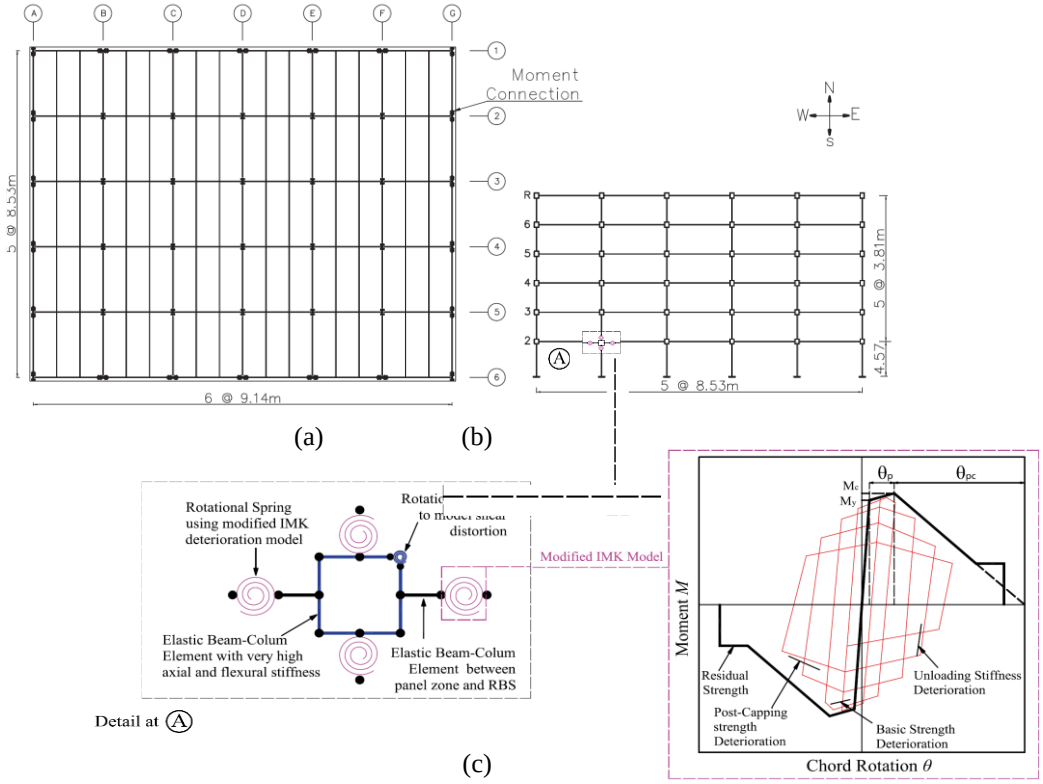


Figure 9. 6-story steel special moment-resisting frame: (a) Plan (b) elevation of 6-story steel special moment-resisting frame (c) modeling details.

Downloaded From: https://www.spiedigitallibrary.org/conference-proceedings-of-spie on 29 Jun 2022
Terms of Use: https://www.spiedigitallibrary.org/terms-of-use

The numerical model of the steel frame building is developed in 2D using the nonlinear seismic analysis program OpenSees (56). In the Opensees, the mass of each floor is introduced to the programming, then after running the code, Opensees assigns the mass of each floor to all nodes for each floor. Also, since all analysis was executed for 2-D models, the mass location effects has not discussed in this study and were ignored. Based on the concentrated plasticity concept, the beam and column elements are modeled with elastic beam-column elements connected by zero-length inelastic plastic hinges employing the modified Ibarra- Krawinkler deterioration model (57, 58). The parameters of the Krawinkler model were obtained for each W-section. The hysteretic behavior of rotational springs is based on the modified Ibarra-Medina Krawinkler (IMK) model which considers the cyclic strength and stiffness deterioration associated with structural damage. The model parameters of backbone curves in IMK model for steel components can be obtained from empirical equations based on calibrated experimental data. First, the offsets for RBS were calculated manually for each beam section. After we obtained the location of the RBS for each W-section, based on the AISE 358, reduced beam sections were modeled using the Krawinkler model by obtaining the necessary parameters of the model. The modified Ibarra-Krawinkler deterioration model considers bilinear hysteric response behavior. The cyclic deterioration model parameters of the zero-length rotational springs are assigned based on the model parameters developed by Lignos and Krawinkler (59). The deterioration characteristics of the rotational springs are indicated by yield strength, post-capping strength, unloading stiffness, and reloading stiffness. The moment-rotation curve is characterized by elastic stiffness, plastic rotation, a post-capping plastic rotation capacity, and the corresponding residual strength. The yield stress of structural steel is assumed to be equal to 375 MPa. To capture the important panel zone deformation modes, the panel zones are modeled considering the shear distortion in beam-column joints using the Krawinkler model (60). The Krawinkler model includes four rigid links and a rotational spring at the upper right corner to represent shear distortion in the panel zone. The nonlinear plastic hinges are created in beams at an offset from the interface of the panel zone and the beam element, while the column plastic hinges are assigned at the face of the panel zone and the column element. To account for P-delta effects, a leaning column is linked to each model with elastic beam-column elements and connected to the model with an axially rigid truss element at each story level. The model assumes Rayleigh damping with a 2% damping ratio for the first and third modes. Using the site's spectral acceleration values, the target spectra for the DBE and MCE levels are developed. A total of 7 ground motions is selected from the PEER NGA database (61), as shown in Table 1, and scaled according to ASCE 7-10. In particular, the ground motions are scaled such that the average response spectra for the selected records are not less than the target response spectrum for periods ranging between 0.2 and 1.5 times the building fundamental period. The steel members of the nine-story building are selected in accordance with the strength requirements of ANSI/AISC 360–10
(55) under the load combinations provided in ASCE 7-10.

The building is also designed to comply with the drift requirements of ASCE 7-10. Since a nonlinear response history is adopted for the design, the allowable story drift is increased by 25% and determined from ASCE 7-10 for Risk Category II buildings as 2.5% under DBE level and as 3.75% under MCE level. The selected column and beam sections for the nine-story frame are shown in

Table *2*. The building satisfies the drift requirements under both DBE and MCE levels, as will be illustrated below. The first mode period of the six and nine-story special moment resisting frames are 2.04s and 2.37 s, respectively.

Table 1. Seven ground motion records used in the design

No.	Earthquake	Station name	Magnitude (M_w)	Distance (km)	Peak ground acceleration (g)
1	Northridge (1994)	Canyon Country	6.7	12.4	0.40
2	Kocaeli, Turkey (1999)	Bolu	7.5	15.4	0.36
3	Superstition Hills-02 (1987)	El Centro Imp.	6.5	18.2	0.26
4	San Fernando (1971)	LA-Hollywood	6.6	22.8	0.19
5	Duzce, Turkey (1999)	Duzce	7.1	12.0	0.81
6	Loma Prieta (1989)	Gilroy Array	6.9	12.2	0.37
7	Imperial valley-06 (1979)	El Centro array	6.5	12.6	0.37

Downloaded From: https://www.spiedigitallibrary.org/conference-proceedings-of-spie on 29 Jun 2022
Terms of Use: https://www.spiedigitallibrary.org/terms-of-use

Table 2. Members of nine-story steel moment-resisting frames

SMRF			SMRF with SMARD	
Story	Exterior/Interior Columns	Girders	Exterior/Interior Columns	Girders
1	W18x311	W21x201	W18x311	W21x201
2	W18x311	W21x201	W18x311	W21x201
3	W18x311	W21x201	W18x283	W21x182
4	W18x311	W21x201	W18x283	W21x182
5	W18x283	W21x182	W18x234	W18x192
6	W18x283	W21x182	W18x234	W18x192

4.2. Steel moment frame with SMARDs

In order to design the six-story frame with damping systems, a reduced strength version of the full code compliant frame is developed first. In particular, the beam and column member sizes are reduced such that the steel frame satisfies the strength requirements of the design codes but does not meet the drift limits. In this more flexible frame, the added dampers will carry a larger portion of the seismic loads and will be mainly responsible for controlling the story drifts. Table 2 provides the selected member sizes for the reduced strength frame. The reduced-strength steel frame is first upgraded with SMARDs to comply with the story drift requirements of ASCE 7-10. In particular, the steel frame with SMARDs is designed using the nonlinear response history procedure and following the seismic design requirements for structures with damping systems described in Chapter 18 of ASCE 7-10.

The experimental data of NiTiHfPd SMA bars for three temperatures, 5°C, -35°C, and 25°C (room temperature), at the loading frequency of 1.0 Hz were shown in Figure 10. To model the hysteretic response of NiTiHfPd SMAs and friction springs, a mechanical model is presented in Open System for Earthquake Engineering Simulation (OpenSees) (56). The model consists of two self-centering materials placed in parallel for the SMAs, as shown in Figure 11(a). The use of two self-centering elements instead of one for the SMAs provides more accurate modeling of the material response, especially for inner loops. Since the SMAs will be subjected to dynamic loading during an earthquake, the experimental responses of SMAs at 1.0 Hz are used for the numerical modeling. The selected parameters of the presented model under the three temperatures of 25°C, 5°C, and -35°C are given in Table 3. Figure 11(b-d) shows the hysteretic curves predicted by the presented model and experimental response at the temperature of 25°C, 5°C, and -35°C for the SMAS. Figure 11(e-f) also shows the model and experimental response for friction spring. The model consists of one self-centering material for friction spring. It can be seen that the two suggested models can predict the response of NiTiHfPd SMA Material very well. The numerical modeling parameters of SMA at room temperature, 25°C, and loading frequency of 1.0 Hz were used in the proposed device.

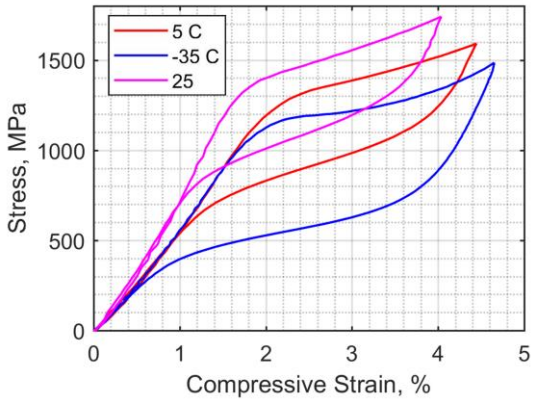


Figure 10. Stress-strain plots of NiTiHfPd SMA bars in three different temperatures and loading frequency of 1.0 Hz

Downloaded From: https://www.spiedigitallibrary.org/conference-proceedings-of-spie on 29 Jun 2022
Terms of Use: https://www.spiedigitallibrary.org/terms-of-use

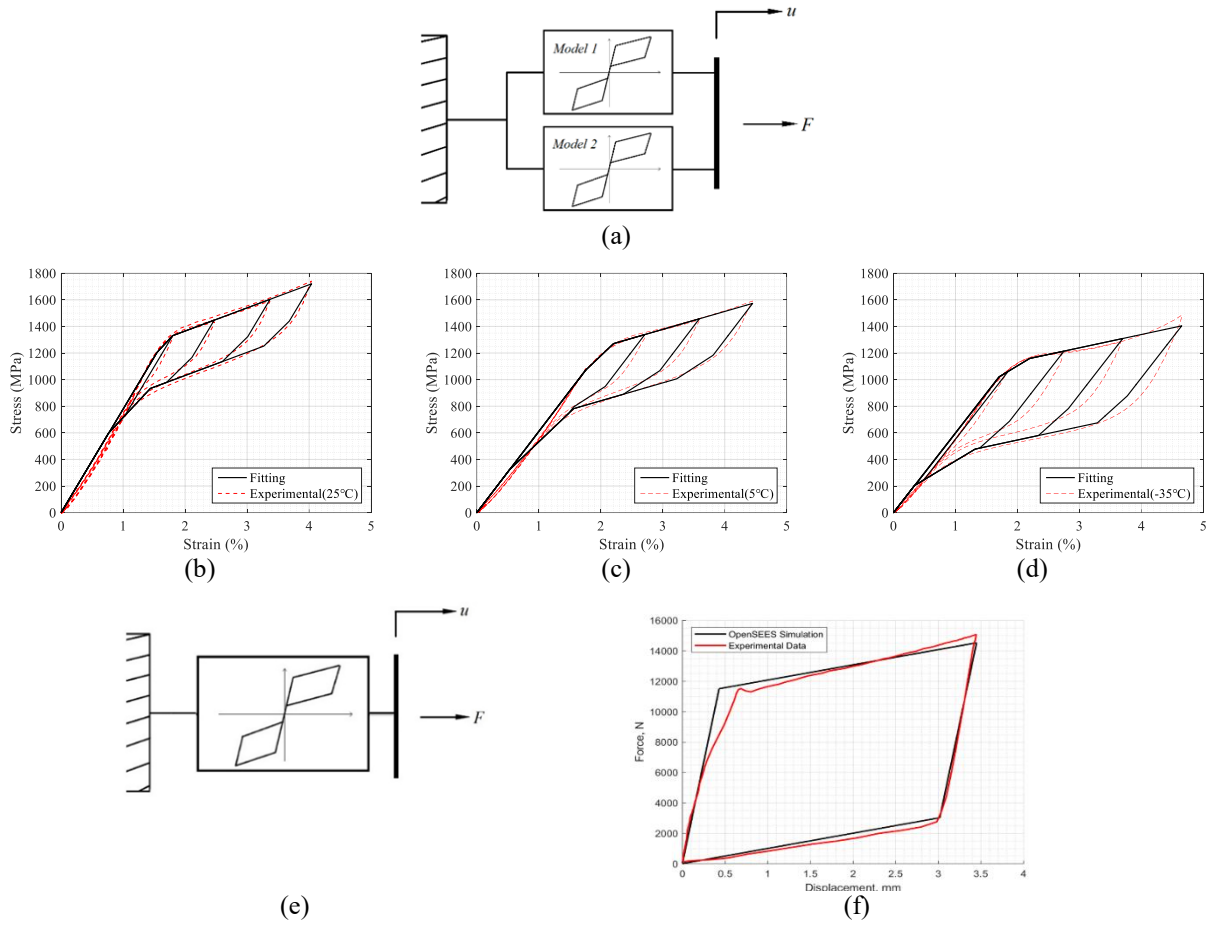


Figure 11. (a) A graphical description of the SMA bar model, and (b) the laboratory strain-stress curve and model estimation for SMA at (b) 25°C, (c) 5°C, and (d) -35°C. (e)A visual illustration of a friction spring and (f) an empirical force-deformation curve and model estimation for a Friction Spring (FS)

Table 3. Parameters of the presented SMA model

Temperature	**25°C**		**5°C**		**-35°C**	
Model	1	2	1	2	1	2
Initial stiffness (MPa/%)	370	410	234.4	377	370	230
Post-transformation stiffness (MPa/%)	87	87	67.4	67.4	50	50
Post-transformation stiffness (MPa/%)	570	738	410.2	829.4	629	505
Ratio of forward to reverse activation stress (β)	0.50	0.20	0.70	0.29	0.80	0.40

The experimental test results of SMAs and friction spring must be modeled in order to be able to use in numerical analysis. There are various methods suggested by researchers to model re-centering materials. Artificial Neural Network (ANN) is one of the most accurate methods for the modeling (62-65). For our purposes, remarkable accurate modeling is not necessary. That being said, the model of the shape memory alloy-based re-centering damper is developed in OpenSees by combining two finite-length elements with uniaxial self- centering material property on representing the SMAs and one finite length element with uniaxial self- centering material property on modeling the friction spring compound. The self-centering material exhibits a flag-shaped hysteric response and captures the post-transformation hardening behavior with a post-hardening stiffness equals to the initial stiffness. The experimental test results of SMAs and friction spring compounds are used to develop model parameters (see Figure 11) for the SMA

Downloaded From: https://www.spiedigitallibrary.org/conference-proceedings-of-spie on 29 Jun 2022
Terms of Use: https://www.spiedigitallibrary.org/terms-of-use

and friction spring compound. The selected parameters for the self-centering material model of the SMAs are as follows: initial stiffness k_1 = 61.23 kN/mm, post-activation stiffness k_2 = 13.80 kN/mm, the ratio of post-transformation hardening stiffness to initial stiffness γ =1.0, forward activation force F_a=104.01 kN and the ratio of forward to reverse activation force β=0.35. The selected parameters for the self-centering material model of the friction springs are as follows: initial stiffness k_1 = 28.75 kN/mm, post-activation stiffness k_2 = 0.9677 kN/mm, ratio of post-transformation hardening stiffness to initial stiffness γ =1.0, forward activation force F_a=11.50 kN and ratio of forward to reverse activation force β=1.0 (see

Table 4).

Table 4. The selected parameters for the self-centering material model of the SMAs and Friction Springs (FS)

Component	**Selected Parameters**				
	k_1 (kN/mm)	k_2 (kN/mm)	γ	F_a (kN)	β
SMAs	61.23	13.80	1.0	104.01	0.35
Friction Springs (FS)	28.75	0.9677	1.0	11.50	1.0

For the six-story building, the SMARDs are installed at two bays at each story level. The design parameters described in Section 6 are used for the SMARDs, and these properties are set to be fixed for each device. The same number of dampers are assumed to be installed at each bay of a given floor. According to Figure 12, the SMARDs are installed at the second and fourth bay of each story level using a chevron brace configuration. Because the SMARD device has high force capacity, the number of dampers for each story is selected to be 2 to satisfy the drift requirement. The average response of the building with the installed dampers under the selected seven ground motions satisfies the member strength criteria and 2% drift requirements of the ASCE/SEI 7-10. The fundamental period of the six-story steel frame with the installed damper is 1.29 s. From the nonlinear time history analyses, the number of dampers for each story is selected to be two to meet the drift requirements.

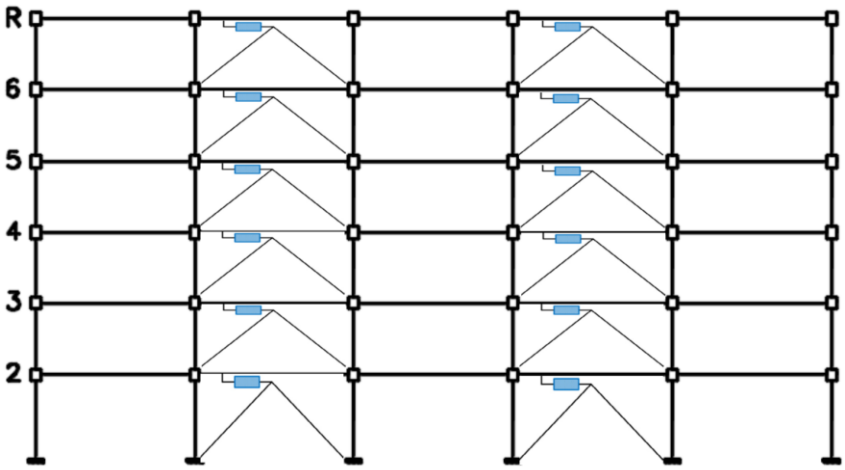


Figure 12. SMARD device installed into a six-story steel frame

Figure 13. (Left) SMARD device installed into the nine-story steel frame, (right) Three-dimensional rendering of SMARD

The mean story drifts for the SMRF, and the steel frame with SMARDs under seven design ground motions are provided in

Table 5 for the DBE and MCE levels. Note that each frame is designed such that the peak inter-story drift obtained from the nonlinear response history procedure meets the code drift requirements without aiming to achieve any higher seismic performance objective.

Downloaded From: https://www.spiedigitallibrary.org/conference-proceedings-of-spie on 29 Jun 2022
Terms of Use: https://www.spiedigitallibrary.org/terms-of-use

Table 5. Drift response of developed frames under design earthquake records

Model	T_1 (s)	Mean inter-story drift			
		DBE		MCE	
		Design (%)	Limit (%)	Limit (%)	Limit (%)
SMRF (6-story)	2.04	2.38	2.5	3.21	3.75
SMRF (9-story)	2.37	2.44		3.25	
6-story SMARDs	1.29	2.34		3.19	
9-story SMARDs	2.19	2.39		3.51	

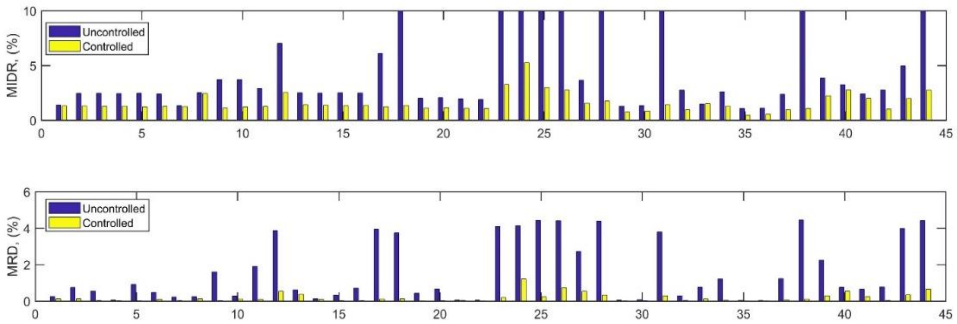
5. PERFORMANCE ASSESSMENT OF THE BUILDINGS

In this study, a set of 22 far-field ground motion pairs used in the FEMA P695 methodology (66) is employed in this study for extensive nonlinear time history analyses for both building. The set represents strong ground motions with PGA N 0.2 g and PGV N 15 cm/s that range in event magnitude from M6.5 to M7.6 and from stiff soils (site Class D) and very stiff soil sites (site Class C). The ground motions are normalized to eliminate unwarranted variability between records. The ground motion records are collectively scaled to selected hazard level, as defined in ASCE/SEI 7-10, such that the median spectral acceleration of the record set matches with those of the design spectra at the fundamental period of each six and nine-story frame (i.e., at 2.04 s for the uncontrolled six-story frame and 1.29 s for the controlled six-story frame. Also, at 2.37 s for the uncontrolled nine-story frame and 2.19 s for the controlled nine-story frame). Peak inter-story drift ratio, which is correlated with damage in structural elements; peak absolute floor acceleration, which is correlated with damage in non-structural components; and peak residual story drift ratio, which is related to the post-earthquake functionality of the structure, are selected as the desired response quantities. Residual story drifts are calculated by continuing the analyses for at least 20s after the end of the seismic event (66, 67). As previous probability-based studies suggested 10%, inter-story drift ratio is considered to define the collapse in numerical simulations (67, 68).

5.1. six-story building

Structural responses of the uncontrolled building and the building with installed SMAs based dampers are computed under each ground motion record at two seismic hazard levels. Figure 14 illustrates the peak inter-story drift ratio, peak residual inter-story drift ratio, and peak floor absolute acceleration for the uncontrolled and controlled buildings under DBE level ground motion records. Figure 15 also demonstrates the peak inter-story drift ratio, peak residual inter-story drift ratio, and peak floor absolute acceleration for the uncontrolled and controlled buildings under MCE level ground motion records. It can be seen that the installed SMARDs reduces the drift demand of the six-story building under all DBE level earthquakes. For uncontrolled structures, the failure of the building is observed under nine ground motion records at the DBE level.

For the controlled structure, the peak inter-story drift ratio is reduced below 3.25% during the same ground motions except for one case where the peak inter-story drift ratio is recorded to be 5.25%. Residual story drift over 1% occurred in the uncontrolled building for eighteen earthquake cases. Almost no residual drifts are observed for the controlled building for all ground motion records except for earthquake number 24 which peak residual drift is 1.24%. Still, peak story accelerations are moderately increased for the controlled building in most of the cases.



Downloaded From: https://www.spiedigitallibrary.org/conference-proceedings-of-spie on 29 Jun 2022
Terms of Use: https://www.spiedigitallibrary.org/terms-of-use

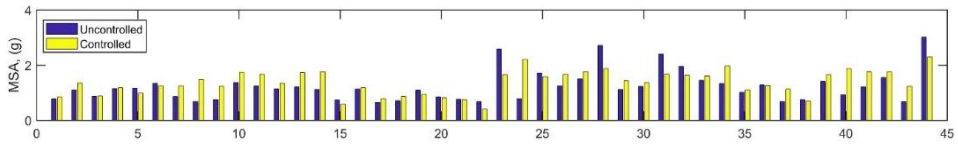


Figure 14. Max inter-story drift, Max residual story drift, and Max floor acceleration for individual DBE level ground motions.

For MCE level seismic hazard, the number of cases where the structure failed is increased dramatically and reached seventeen for the uncontrolled building, although the collapse is observed only once for the controlled building. It can be observed that the uncontrolled building experience large permanent drifts for twenty-eight ground motion cases, which is remarkable. On the other hand, the building upgraded with SMARDs has minimal residual drifts for most cases. Similar to the DBE level hazard, the controlled structure has a higher acceleration response for more than half of the ground motion record cases

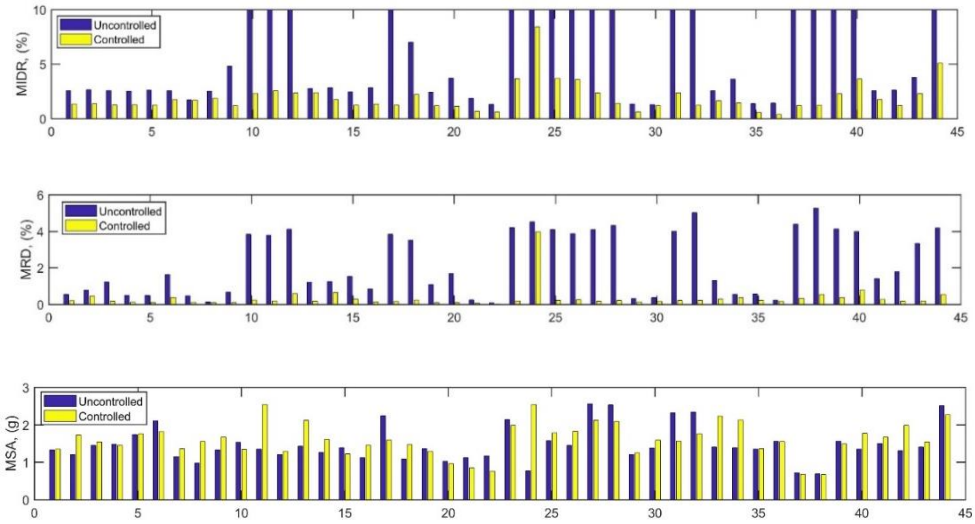


Figure 15. Peak inter-story drift, max residual story drift, and max floor acceleration for individual MCE level ground motions.

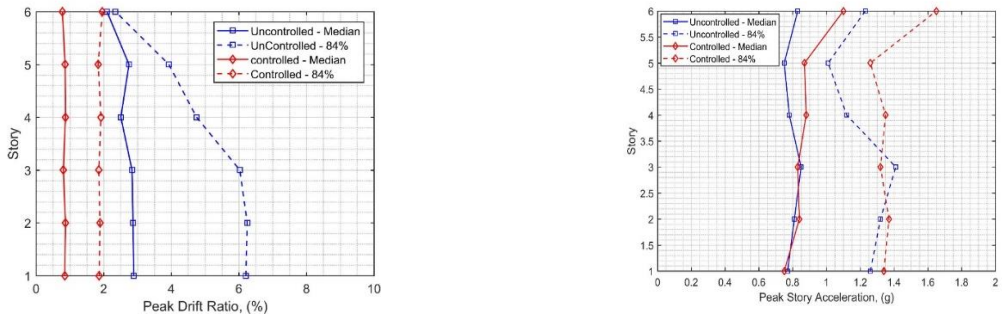
As the distribution of the seismic response is typically assumed to follow a lognormal distribution, the statistics of the peak inter-story drift ratio and peak story absolute acceleration response under 44 ground motion records are provided in terms of the median (50 percentile) and 84 percentile response and calculated as equations (3-4):

$$\hat{X} = \exp\left(\frac{\sum_{i=1}^{n} \ln x_i}{n}\right) \quad (3)$$

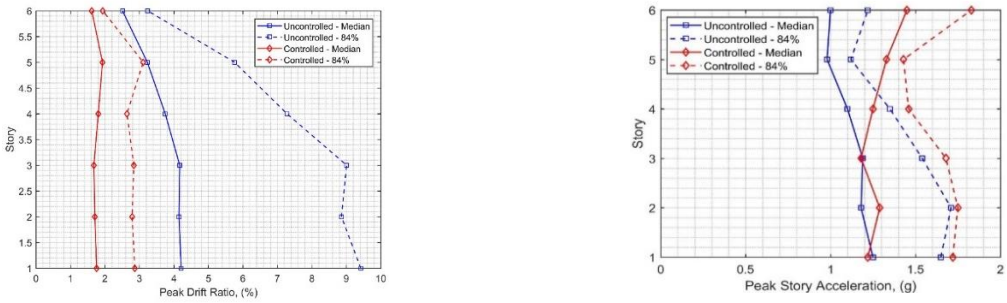
$$X^{84} = \hat{X} \exp\left(\sigma_{\ln X}\right) \quad (4)$$

where n is the number of response data points and σ_{lnX} is the standard deviation of the logarithm of response X. Figure 16 shows the median and 84-percentile values of the peak inter-story drift ratio and peak story absolute acceleration at each floor level for the uncontrolled and controlled buildings to the DBE and MCE levels.

Downloaded From: https://www.spiedigitallibrary.org/conference-proceedings-of-spie on 29 Jun 2022
Terms of Use: https://www.spiedigitallibrary.org/terms-of-use



(a)



(b)

Figure 16. Statistics of max story absolute acceleration and max inter-story drift ratio for unprotected and controlled structures exposed to 44 earthquakes at the (a) DBE and (b) MCE levels

It can be discerned that peak inter-story drift attains smaller values for the controlled structure at all the floors for both DBE and MCE hazard levels. The peak median peak inter-story drift ratio reaches about 2.89% and 4.21% for the uncontrolled structure for the DBE and MCE levels, respectively. On the other hand, the median peak inter-story drift ratio is uniformly distributed along with the height of the structure for the controlled frame with a maximum of 0.87% and 1.93% for the DBE and MCE levels, respectively. That clearly shows the effectiveness of SMARDs in reducing the displacement response of the steel building, especially at high seismic hazard levels. Moreover, the maximum 84-percentile inter-story drift ratios for the conventional frame are 6.25% and 9.42% for the DBE and MCE, respectively. The corresponding values are only 1.92% and 3.11% for the steel frame with SMARDs.

The peak acceleration response moderately goes up for the steel frame with the installed SMARD dampers. The peak median accelerations for the uncontrolled frame are 0.85 g and 1.25 g, and the peak 84-percentile acceleration values are 1.32 g and 1.71 g for the DBE and MCE, respectively. For the controlled frame, the median values are 0.88 g and 1.45 g at DBE, and the peak 84-percentile acceleration values are 1.65 g and 1.83 g at MCE.

6. CONCLUSIONS

In this paper, NiTiHfPd alloy plus friction spring are employed, as two essential compounds of a structural passive control system, in 6-story steel frame building to provide re-centering and energy-dissipating capabilities. First, experimental tests on NiTiHfPd alloys that have ultra-high-strength, large damping capacity, and a wide operating temperature range are discussed. The impact of different ranges of temperatures on the mechanical behavior of the SMA bars is explored. Also, experimental tests on friction springs that have the high force and deformation capacity are discussed. A super-elastic memory alloy re-centering damper device, which advantages the inherent re-centering capability of high-performance SMA bars and high energy dissipation ability of friction spring compound for superior seismic performance, is proposed in this study. A high damped friction spring compound, which provides high damping as well as high deformation capability, is considered for the re-centering and energy dissipation component of the hybrid damper, named as super-elastic memory alloy re-centering damper.

Experimental tests on the subcomponents of the SMARD device, i.e., friction spring compound and high-performance SMA bars, are carried out to characterize their mechanical response. Performance and effectiveness of the proposed damper in mitigating response of steel frame buildings under DBE and MCE level seismic loads are

Downloaded From: https://www.spiedigitallibrary.org/conference-proceedings-of-spie on 29 Jun 2022
Terms of Use: https://www.spiedigitallibrary.org/terms-of-use

assessed through numerical studies. A six-story special steel moment frame structure is modeled as a conventional moment-resisting frame and the frame with installed as super-elastic memory alloy re-centering dampers. A suite of 44 strong ground motion records are normalized and scaled as described in FEMA P695. Nonlinear response history analyses are conducted, and the peak response quantities are evaluated. Results show that the inter-story drift demands and residual drifts of the building subjected to DBE and MCE level earthquakes can significantly be reduced with installed SMARDs without a considerable increase in peak acceleration demand. However, future studies are needed to experimentally verify the response of the proposed device and study the effect of temperature on the response of the hybrid device.

Acknowledgments

This material is based upon the work supported by the National Science Foundation under Grant Number CMMI-1538770. The author of the paper also thanks to my colleagues from the Department of Material Science at the University of Kentucky, who provided experimental data that greatly assisted the research.

REFERENCES

1. ANSI A. AISC 341-05. Seismic provisions for structural steel buildings Chicago (IL): American Institute of Steel Construction. 2005.
2. Uma SR, Pampanin S, Christopoulos C. Development of Probabilistic Framework for Performance-Based Seismic Assessment of Structures Considering Residual Deformations. Journal of Earthquake Engineering. 2010;14(7):1092-111.
3. Bojórquez E, Ruiz-García J. Residual drift demands in moment-resisting steel frames subjected to narrow-band earthquake ground motions. Earthquake engineering & structural dynamics. 2013;42(11):1583-98.
4. El-Sheikh MT, Sause R, Pessiki S, Lu L-W. Seismic behavior and design of unbonded post-tensioned precast concrete frames. PCI journal. 1999;44(3):54-71.
5. Ricles JM, Sause R, Garlock MM, Zhao C. Posttensioned seismic-resistant connections for steel frames. Journal of Structural Engineering. 2001;127(2):113-21.
6. Perez FJ, Sause R, Pessiki S. Analytical and experimental lateral load behavior of unbonded posttensioned precast concrete walls. Journal of Structural Engineering. 2007;133(11):1531-40.
7. Christopoulos C, Filiatrault A, Uang C-M, Folz B. Posttensioned energy dissipating connections for moment-resisting steel frames. Journal of Structural Engineering. 2002;128(9):1111-20.
8. Eatherton M, Hajjar J, Deierlein G, Ma X, Krawinkler H, editors. Hybrid simulation testing of a controlled rocking steel braced frame system. 9 th US National and 10 th Canadian Conference on Earthquake Engineering, Toronto; 2010.
9. Christopoulos C, Tremblay R, Kim H-J, Lacerte M. Self-centering energy dissipative bracing system for the seismic resistance of structures: development and validation. Journal of structural engineering. 2008;134(1):96-107.
10. Chancellor NB, Eatherton MR, Roke DA, Akbaş T. Self-Centering seismic lateral force resisting systems: high performance structures for the city of tomorrow. Buildings. 2014;4(3):520-48.
11. Ozbulut OE, Hurlebaus S, DesRoches R. Seismic response control using shape memory alloys: a review. Journal of Intelligent Material Systems and Structures. 2011;22(14):1531-49.
12. Qian H, Li H, Song G, Guo W. Recentering shape memory alloy passive damper for structural vibration control. Mathematical Problems in Engineering. 2013;2013.
13. Araki Y, Endo T, Omori T, Sutou Y, Koetaka Y, Kainuma R, et al. Potential of superelastic Cu–Al–Mn alloy bars for seismic applications. Earthquake Engineering & Structural Dynamics. 2011;40(1):107-15.
14. Araki Y, Maekawa N, Shrestha KC, Yamakawa M, Koetaka Y, Omori T, et al. Feasibility of tension braces using Cu–Al–Mn superelastic alloy bars. Structural Control and Health Monitoring. 2014;21(10):1304-15.
15. Ozbulut O, Mir C, Moroni M, Sarrazin M, Roschke P. A fuzzy model of superelastic shape memory alloys for vibration control in civil engineering applications. Smart materials and structures. 2007;16(3):818.
16. Parulekar Y, Reddy G, Vaze K, Guha S, Gupta C, Muthumani K, et al. Seismic response attenuation of structures using shape memory alloy dampers. Structural control and health monitoring. 2012;19(1):102-19.
17. Motahari S, Ghassemieh M, Abolmaali S. Implementation of shape memory alloy dampers for passive control of structures subjected to seismic excitations. Journal of Constructional Steel Research. 2007;63(12):1570-9.
18. Symans M, Charney F, Whittaker A, Constantinou M, Kircher C, Johnson M, et al. Energy dissipation systems for seismic applications: current practice and recent developments. Journal of structural engineering. 2008;134(1):3-21.
19. Wang J, Zhao H. High performance damage-resistant seismic resistant structural systems for sustainable and resilient city: A review. Shock and Vibration. 2018;2018.
20. Takagi J, Wada A. Recent earthquakes and the need for a new philosophy for earthquake-resistant design. Soil Dynamics and Earthquake Engineering. 2019;119:499-507.

Downloaded From: https://www.spiedigitallibrary.org/conference-proceedings-of-spie on 29 Jun 2022
Terms of Use: https://www.spiedigitallibrary.org/terms-of-use

21. Soong TT, Dargush GF. * Passive Energy Dissipation Systems in Structural Engineering: Wiley; 1997.
22. Li Z, Shu G, Huang Z. Development and cyclic testing of an innovative shear-bending combined metallic damper. Journal of Constructional Steel Research. 2019;158:28-40.
23. Mashal M, Palermo A, Keats G. Innovative metallic dissipaters for earthquake protection of structural and non-structural components. Soil Dynamics and Earthquake Engineering. 2019;116:31-42.
24. Marshall JD, Charney FA. Seismic response of steel frame structures with hybrid passive control systems. Earthquake engineering & structural dynamics. 2012;41(4):715-33.
25. Wang C-L, Liu Y, Zheng X, Wu J. Experimental investigation of a precast concrete connection with all-steel bamboo-shaped energy dissipaters. Engineering Structures. 2019;178:298-308.
26. Liu Y, Wang C-L, Wu J. Development of a new partially restrained energy dissipater: Experimental and numerical analyses. Journal of Constructional Steel Research. 2018;147:367-79.
27. Qiu C-X, Zhu S. Performance-based seismic design of self-centering steel frames with SMA-based braces. Engineering Structures. 2017;130:67-82.
28. Gao N, Jeon J-S, Hodgson DE, DesRoches R. An innovative seismic bracing system based on a superelastic shape memory alloy ring. Smart materials and structures. 2016;25(5):055030.
29. Ozbulut O, Roschke P, Lin P, Loh C. GA-based optimum design of a shape memory alloy device for seismic response mitigation. Smart Materials and Structures. 2010;19(6):065004.
30. Ozbulut OE, Hurlebaus S. Application of an SMA-based hybrid control device to 20-story nonlinear benchmark building. Earthquake Engineering & Structural Dynamics. 2012;41(13):1831-43.
31. Mishra SK, Gur S, Chakraborty S. An improved tuned mass damper (SMA-TMD) assisted by a shape memory alloy spring. Smart Materials and Structures. 2013;22(9):095016.
32. Parulekar Y, Kiran AR, Reddy G, Singh R, Vaze K. Shake table tests and analytical simulations of a steel structure with shape memory alloy dampers. Smart materials and structures. 2014;23(12):125002.
33. Ozbulut OE, Hurlebaus S. A comparative study on the seismic performance of superelastic-friction base isolators against near-field earthquakes. Earthquake Spectra. 2012;28(3):1147-63.
34. Ozbulut O, Hurlebaus S. Energy-balance assessment of shape memory alloy-based seismic isolation devices. Smart Structures and Systems. 2011;8(4):399-412.
35. Ozbulut OE, Hurlebaus S. Seismic assessment of bridge structures isolated by a shape memory alloy/rubber-based isolation system. Smart Materials and Structures. 2010;20(1):015003.
36. Dezfuli FH, Alam MS. Shape memory alloy wire-based smart natural rubber bearing. Smart Materials and Structures. 2013;22(4):045013.
37. Ghodke S, Jangid R. Influence of high austenite stiffness of shape memory alloy on the response of base-isolated benchmark building. Structural Control and Health Monitoring. 2017;24(2):e1867.
38. Dolce M, Cardone D, Marnetto R. Implementation and testing of passive control devices based on shape memory alloys. Earthquake engineering & structural dynamics. 2000;29(7):945-68.
39. Zhu S, Zhang Y. Seismic behaviour of self-centring braced frame buildings with reusable hysteretic damping brace. Earthquake engineering & structural dynamics. 2007;36(10):1329-46.
40. Ozbulut OE, Hurlebaus S. Re-centering variable friction device for vibration control of structures subjected to near-field earthquakes. Mechanical Systems and Signal Processing. 2011;25(8):2849-62.
41. Ozbulut OE, Bitaraf M, Hurlebaus S. Adaptive control of base-isolated structures against near-field earthquakes using variable friction dampers. Engineering Structures. 2011;33(12):3143-54.
42. Yang C-SW, DesRoches R, Leon RT. Design and analysis of braced frames with shape memory alloy and energy-absorbing hybrid devices. Engineering Structures. 2010;32(2):498-507.
43. Silwal B, Michael RJ, Ozbulut OE. A superelastic viscous damper for enhanced seismic performance of steel moment frames. Engineering Structures. 2015;105:152-64.
44. Silwal B, Ozbulut OE, Michael RJ. Seismic collapse evaluation of steel moment resisting frames with superelastic viscous damper. Journal of Constructional Steel Research. 2016;126:26-36.
45. Miller DJ, Fahnestock LA, Eatherton MR. Development and experimental validation of a nickel–titanium shape memory alloy self-centering buckling-restrained brace. Engineering Structures. 2012;40:288-98.
46. Wang B, Zhu S. Cyclic tension–compression behavior of superelastic shape memory alloy bars with buckling-restrained devices. Construction and Building Materials. 2018;186:103-13.
47. Qiu C, Fang C, Liang D, Du X, Yam MC. Behavior and application of self-centering dampers equipped with buckling-restrained SMA bars. Smart Materials and Structures. 2020;29(3):035009.
48. Acar E, Tobe H, Karaca H, Noebe R, Chumlyakov Y. Microstructure and shape memory behavior of [111]-oriented NiTiHfPd alloys. Smart Materials and Structures. 2016;25(3):035011.
49. Shi F, Toker G, Dizaji FS, Ozbulut O, Karaca H, editors. Experimental and numerical investigations on seismic applications of high damping smas. Proceeding in Eleventh US National Conference on Earthquake EngineeringIntegrating Science, Engineering & Policy; 2018.
50. Filiatrault A, Tremblay R, Kar R. Performance evaluation of friction spring seismic damper. Journal of Structural Engineering. 2000;126(4):491-9.
51. Saedi S, Dizaji FS, Ozbulut OE, Karaca HE. Structural vibration control using high strength and damping capacity shape memory alloys. Dynamics of Civil Structures, Volume 2: Springer; 2017. p. 259-66.

Downloaded From: https://www.spiedigitallibrary.org/conference-proceedings-of-spie on 29 Jun 2022
Terms of Use: https://www.spiedigitallibrary.org/terms-of-use

52. Dizaji FS, Dizaji MS. A Novel Smart Memory Alloy Re-centering Damper for Passive Protection of Structures Subjected to Seismic Excitations Using High-Performance NiTiHfPd Material. arXiv preprint arXiv:210504081. 2021.
53. FEMA P. 751. 2009 NEHRP recommended seismic provisions: Design examples. Building Seismic Safety Council Washington, DC, USA. 2012.
54. ASCE, editor Minimum design loads for buildings and other structures2005: American Society of Civil Engineers.
55. AISC, editor Seismic provisions for structural steel buildings2010: AISC Chicago.
56. Mazzoni S, McKenna F, Scott M, Fenves G. Open System for Earthquake Engineering Simulation,(OpenSEES http://opensees. berkeley. edu/). Pacific Earthquake Engineering Research Center (PEER), Berkeley, California. 2014.
57. Ibarra LF, Medina RA, Krawinkler H. Hysteretic models that incorporate strength and stiffness deterioration. Earthquake engineering & structural dynamics. 2005;34(12):1489-511.
58. Lignos DG, Krawinkler H. Deterioration modeling of steel components in support of collapse prediction of steel moment frames under earthquake loading. Journal of Structural Engineering. 2011;137(11):1291-302.
59. Lignos DG, Krawinkler H. A database in support of modeling of component deterioration for collapse prediction of steel frame structures. Structural Engineering Research Frontiers2007. p. 1-12.
60. Gupta A. Seismic demands for performance evaluation of steel moment resisting frame structures: Stanford University; 1999.
61. Medina R, Krawinkler H. Pacific Earthquake Engineering Research Center. University of California, Berkeley. 2004.
62. Farrokh M, Dizaji MS, Dizaji FS, Moradinasab N. Universal Hysteresis Identification Using Extended Preisach Neural Network. arXiv preprint arXiv:200101559. 2019.
63. Dizaji MS, Dizaji FS. Artificial Neural Networks to Determine Source of Acoustic Emission and Damage Detection. 2017.
64. Dizaji MS, Dizaji FS, Taghizadeh E. Nonlinear Adaptive Simulation of Concrete Gravity Dams using Generalized Prandtl Neural Networks. 2018.
65. Joghataie A, Dizaji MS, Dizaji FS, editors. Neural Network Software for Dam-Reservoir-Foundation Interaction. Proceedings of the International Conference on Mechanical, Automotive and Materials Engineering, Dubai, United Arab Emirates; 2012.
66. FEMA P. Quantification of building seismic performance factors. Washington, DC; 2009.
67. ASCE, editor Minimum design loads for buildings and other structures2010: American Society of Civil Engineers.
68. Ribeiro FL, Barbosa AR, Neves LC. Application of reliability-based robustness assessment of steel moment resisting frame structures under post-mainshock cascading events. Journal of Structural Engineering. 2014;140(8):A4014008.

Downloaded From: https://www.spiedigitallibrary.org/conference-proceedings-of-spie on 29 Jun 2022
Terms of Use: https://www.spiedigitallibrary.org/terms-of-use